Title

A Study on the Dynamic Effects of Active Pitch Control in an Flapping Wing Robot with Elastic Element

Author

Zhu, David

Publication Date

2022

UNIVERSITY OF CALIFORNIA SAN DIEGO

A Study on the Dynamic Effects of Active Pitch Control in an Flapping Wing Robot with Elastic Element

A Thesis submitted in partial satisfaction of the
requirements for the degree Master of Science

in

Mechanical Engineering

by

David Zhu

Committee in charge:

Professor Nicholas Gravish, Chair
Professor John Hwang
Professor Tania Morimoto

2022

The Thesis of David Zhu is approved, and it is acceptable in quality and form for publication on microfilm and electronically.

University of California San Diego

2022

DEDICATION

To my dear colleagues, friends, and family for their utmost support throughout my academic career.

TABLE OF CONTENTS

LIST OF FIGURES

LIST OF TABLES

ACKNOWLEDGEMENTS

Chapter 2 and 4, in part, is based on the work from Dimensional analysis of spring-wing systems reveals performance metrics for resonant flapping-wing flight. By Lynch, James and Gau, Jeffrey and Sponberg, Simon and Gravish, Nick. The work of this thesis utilized the apparatus constructed for this paper.

ABSTRACT OF THE THESIS

A Study on the Dynamic Effects of Active Pitch Control in an Flapping Wing Robot with Elastic Element

by

David Zhu

Master of Science in Mechanical Engineering

University of California San Diego, 2022

Professor Nicholas Gravish, Chair

Elastic components in flapping wing micro-aerial vehicles, or FWMAV, have been a topic of interest for their high dynamic efficiency and energy storage. Previous work has looked at the use of a dynamically scaled robo-physical model to analyze the energetics of a spring-wing system. Both the simulation and experimental analysis reaffirms the advantages of resonance behavior in high frequency wing stroke motion. However, this system, similar to their biological counterparts, suffers from significant energy loss due to damping. A method to accelerate the system's transition into stable resonance is needed. In this vein, the effect of active pitch control during the emergence of resonance behavior in a spring-wing system is analyzed and studied. Simulation of the dynamic model was constructed for kinematic analysis. To validate the hypothesis, a physical robotic apparatus is used to experimentally observe the behavior of the system. We determine the variation in kinematic phase difference between the stroke and pitch angle will result in changes in the effective drag coefficient. The results of this paper can be applied in furthering the development of active pitch locomotion of a FWMAV and studies of insect flight behavior.

Chapter 1

Introduction

1.1 Background

The concept of flight has been a perplexing phenomenon that has intrigued humankind for much of our existence. The invention of aircraft has made that a tangible reality for many people. In recent years, more interest has been put on investigating other means of aerial propulsion beyond the earlier fixed wing airplanes and rotorcraft helicopters, and researchers has found their muse in nature. Birds and flying insects have long been studied with their flight locomotion [5],[22]. Studies have shown the acute advantages of flapping wing locomotion at length scales of 30cm and below [18], with flying insects demonstrating surprising agility for their size. Many researchers hope to imitate their efficient use of energy [22] and robust flight kinematics [20]. Compared to conventional airplanes and rotorcraft, flapping wing micro aerial vehicles, or FWMAV, are able perform diverse sets of flight locomotion and a more energy efficient manner [7].

Works such as the Harvard Robobee [16],[24], and robotic Nano Hummingbird [13] has demonstrated considerable promise in untethered navigation under limited exterior control. However, the scale of these FWMAVs greatly limits their operational capacity. A major challenge lies in their flight kinematics, where stroke reversals of the flapping wing necessities a great deal of power for acceleration and deceleration of the entire wing. The advancement of computational fluid dynamic analysis has made the studying of these unsteady behavior easier [14] as a mean

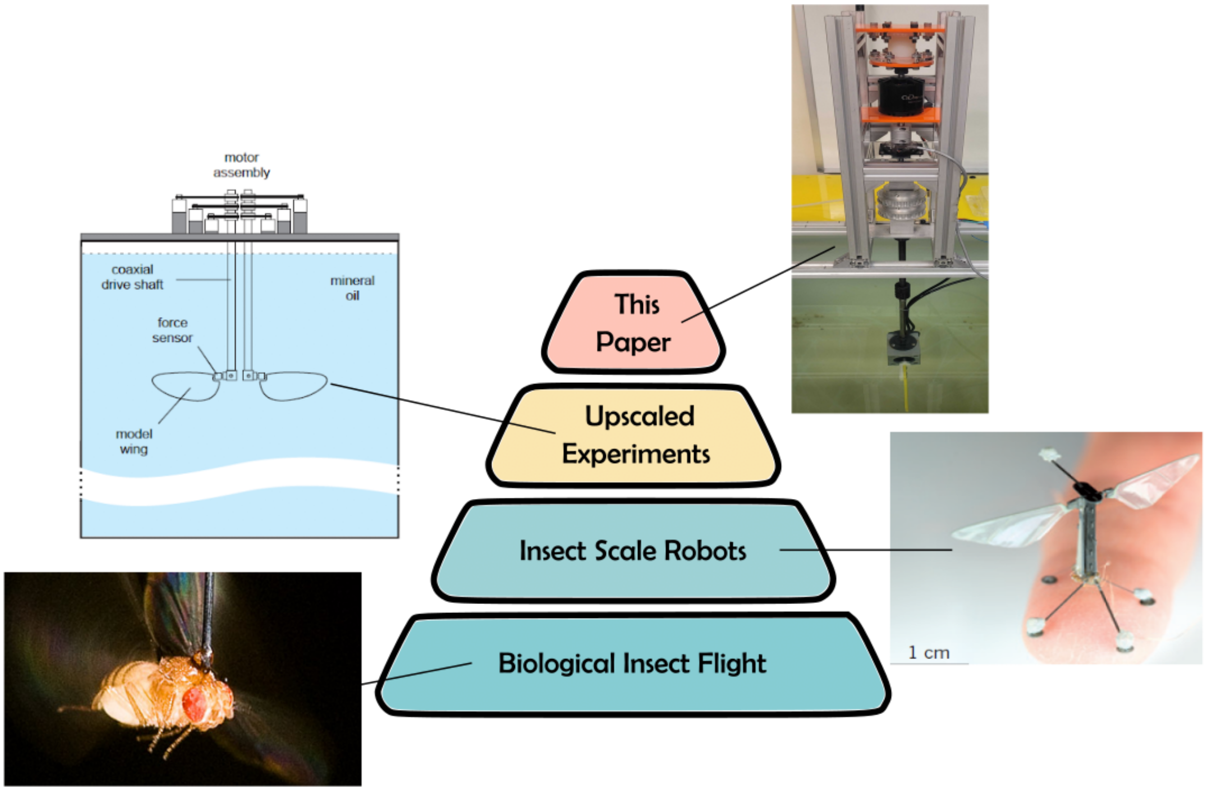

Figure 1.1. The background works leading up to this paper. From biological kinematics and the famous RoboBee[24], to the dynamically scaled experiments from [13]. The work presented in this thesis furthers the study in the fields of FWMAV analysis.

to achieve energy efficient flight. Roboticists has began researching into the advantages of resonance in incorporating elastic springs within the robot's transmission [10]. Others have looked into more systemic analysis on the aerodynamics that made flapping wing flight efficient given their scale and frequency [4].

1.2 Biology of Insect flight

Researchers has long held interest in studying insect flight behavior. Weis-Fogh is considered to be the preeminent entomologist on the subject. His work on the dynamics of insect hovering mechanism and lift production [23] serves as a foundation for much of later work in the same field. More importantly for this paper, his 1960 discovery of resilin within the insect thorax [21] inspired the incorporation of elastic element within FWMAVs. The resilin demonstrate robust properties as an elastic material, capable of rapid excitation that enables high frequency wing beat crucial to insect flight. This extraordinary properties of this new material suggest a wide range of application in biological, medical, and engineering [1].

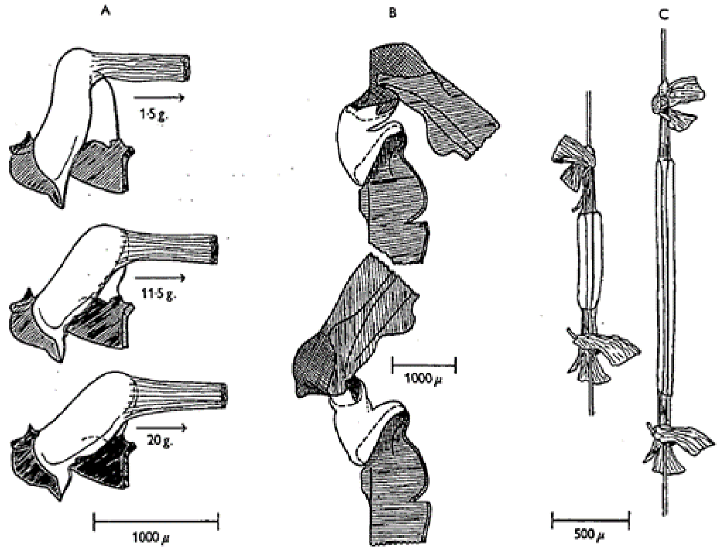

Figure 1.2. Three examples of resilin structures from insect thoraxes. (A) the prealar arm from Schistocerca, or locust, strained by three different loads. (B) The main wing hinge of a locust forewing, resting (above) and strained (below). (C) The elastic tendon of a Aeschna, or dragonfly, unstrained and extended. Figure from [21]

Insect also demonstrate striking control mechanism when in flight. Many birds and larger insect utilize muscles directly connected to the wings for actuation. As the length scale decreases, wing beat frequency greatly increases in order to compensate for lift production [17]. It is within this regime that indirect flight kinematics and asynchronous muscle become a prominent feature. Gau et al. work on indirect flight kinematic further describe the advantages of elastic energy exchange in small scale insect [8]. They found that elastic energy storage in the thorax is critical in hovering flight by decreasing power requirements. By utilizing energy recovery via the scutum region, insects are able increase energy efficiency for flight.

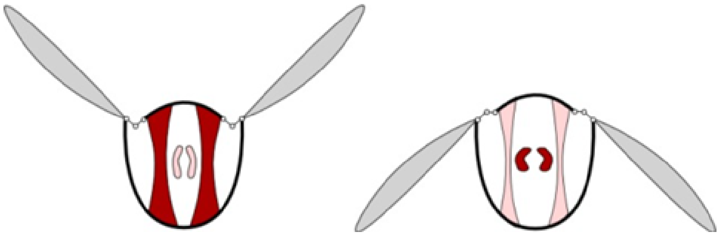

Figure 1.3. Illustration of the operation of an insect's wings using indirect flight muscles. The darker muscles are those in the process of contracting. Figure credited to Amateur Entomologists' Society at amentsoc.org.

Weis-Fogh's work on flight dynamic estimation using the quasi-steady model was a hallmark within the field. But his student Ellington argued that the aerodynamic behavior of flapping wing kinematic should take into account of unsteady behavior of the working fluid [6]. One key mechanism of lift amplification is clip and fling motion, shown in figure 1.4. The first part of the motion, the ”clap”, happens before stroke reversal as the leading edges of the wings touch each other before the trailing edges, thus progressively closing the gap between them. As the wings press together closely, the opposing circulations of each of the airfoils annul each other, which greatly reduce the Wagner effect and extend the generation of lift. Then as the wing pronate and moves back, the leading edges ‘flings’ apart. This creates a region of low pressure for air to quickly fill in, providing an initial impetus to the attached vorticity [18].

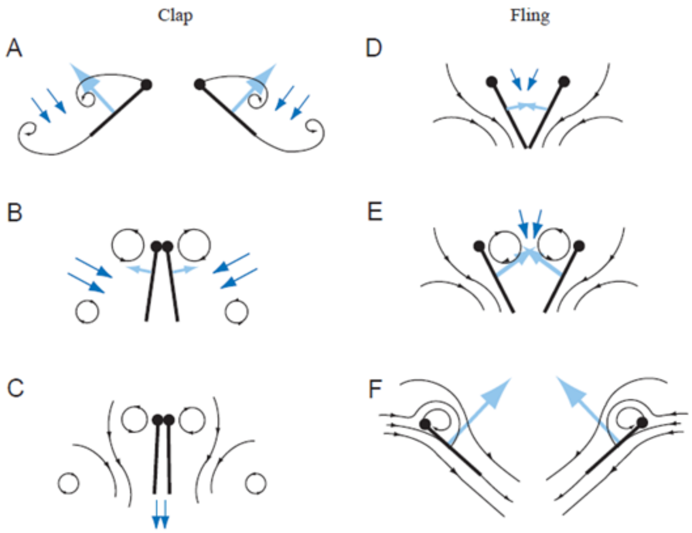

Figure 1.4. Illustration showing the mechanism of the Clap-and-Fling in producing lift. Initially proposed by Weis-Fogh, this flight mechanism allows for the production of higher than previously estimated thrust and reduce influences of Wagner effect. From [18]

1.3 Flapping Wing Robots

Although fixed-wing planes rotocraft drones are still the dominant designs for aerial vehicles, flapping wing as a mechanical design proves to be advantagrous in their scalability. Flapping wing micro aerial vehicles, or FWMAVs for short, are researchers' attempt at mimicking the fascinating locomotive behavior of the insects. These insect-scale robots are capable of complex locomotion given their size by utilizing the above mentioned unsteady aerodynamic behavior [7]. One of the most successful design at replicating flapping wing flight at scale is the Harvard RoboBee 1.5. Utiilizing a piezioelectric actuator with flexture based skeleton, the first RoboBee weights only about 80 milligram and can perform tethered lift-off and basic locomotion[16]. The wings are secured onto a flexible hinge, allowing them to passively pitch in a manner that resembles their biological counterpart [24]. However, its small size greatly limits its loading capability. The early design of the RoboBee have to relie on external power transmission and control. Later iterations of the robot was able to achieve untethered flight using solar panels and on-board electronics, but the design is no longer at the same length and weight scale of insects [11]. Still, the power autonomy allow for great flexibility and feasibility in field applications.

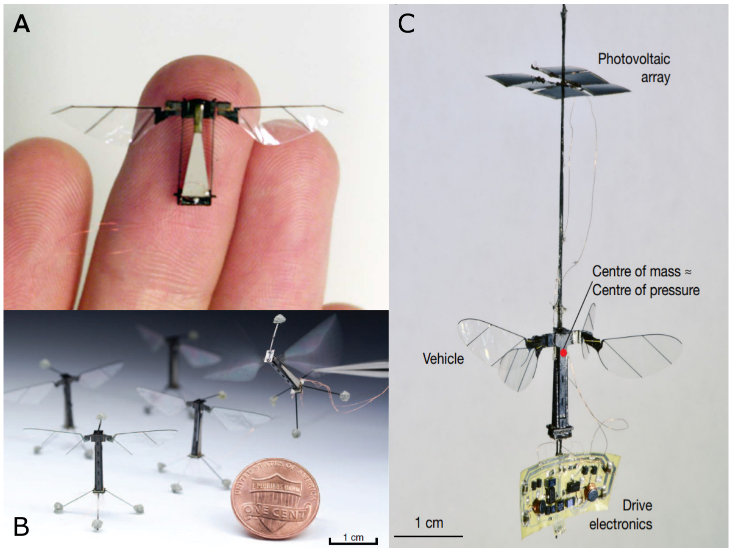

Figure 1.5. Different designs of the RoboBee. (A)The earliest design, which is only capable of lift off on the rod. It resembles insects like bees and fly the most from its appearance and weight. (B)This iteration of the design is capable of independent lift off and basic controlled locomotion. However, it still relie on external means for power and control scheme. (C)The first successful untethered design, with on bard power generation and electronic. Although heavier and longer, its autonomy allowed for a wide range of application. From [24]

Observing the limitation of a conventional transmission, researchers look back into the anatomy of insects for inspiration. One important aspect they borrowed from biology is the use of elastic element within the insect's thorax. Numerical models have shown the advantages of elastic energy exchange at increasing the operation efficiency. Furthermore, the resonance properties of the elastic transmission increase lift and power efficiency when the system is driven at its natural frequency [25]. This prompt roboticists to integrate spring-like elements to their design, an example of which is shown in figure 1.7. Springs are attached in parallel to the two actuators output, allowing the wings to independently operate at resonance. Through experimental iteration, the team was able to achieve a lift-to-weight ratio of 1.4 while operating at the natural frequency of the system[10]. Further work on the design focuses on design improvements on the different wing shape. The compliant design of the wing, which mimics flexible properties of insect wings, shows promise in improving lift production and flight stability [3].

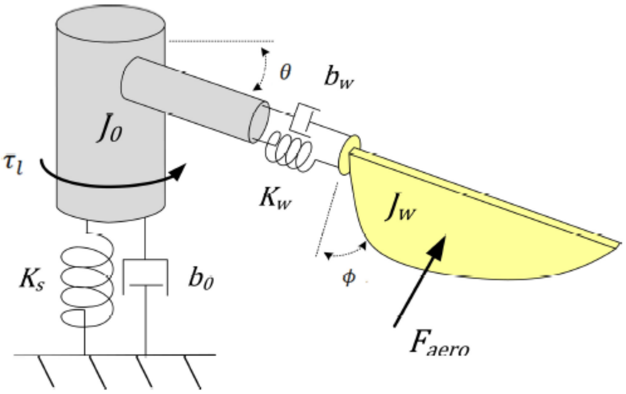

Figure 1.6. Simplified representation of a flipping wing with elastic element as a spring-mass-damper system. The aerodynamic force on the wing acts as a nonlinear damping moment on both the wing rotational and flapping motion. From [10]

Bio-inspired design extends beyond just mimicking the anatomy of insects; Researcher also find utility in their muscle control mechanism. Many small scale insects, like fruit flies,actuates their muscle in an asynchronous manner between electrical and mechanical activity of the muscle. This is enabled by low-level control from the muscle instead of the brain, and exhibit properties such as delayed stretch activation and shortening deactivation [12]. Researcher sought to replicate the delayed stretch activation with a oscillator based central pattern generator [15]. This novel control scheme exhibit oscillation behavior robust against changes in physical parameter and even sudden intrusion. The seemingly compliant nature of the control method allow FWMAVs to operate in hazardous environment.

1.4 Aerodynamic Analysis

Given the difficulty of experimenting on actual insects, many research has instead looked into mimicking insect flight dynamics on larger robots. By using the principle of dynamically scaling, Dickinson and his colleagues built and experimented on a robotics wing system capable

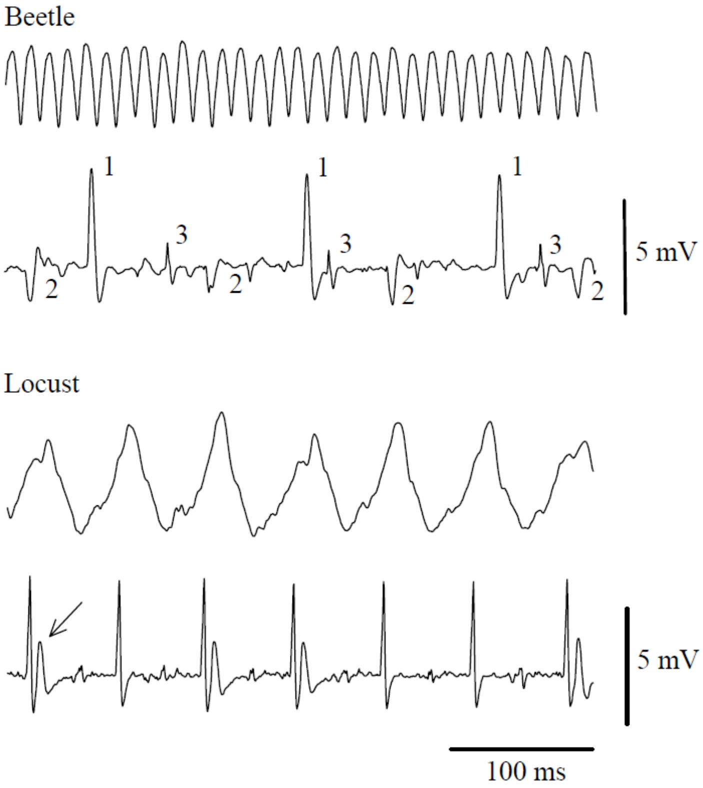

Figure 1.7. Illustration depicting the anatomical difference between direct and indirect flight mechanic. From [2]

of performing various kind of wing stroke and pitch pattern [4],[19]. The robot is placed within a tank of mineral oil, with the size of the wing and wing stroke amplitude carefully chosen in order to confine the system operation within Reynolds number similar to that of insects. By attaching force and displacement sensors, Dickinson was able to establish a general relationship between transnational and rotational mechanisms in lift generation. He points to delayed stall, rotational circulation, and wake capture as the three major mechanism of which lift generation is maximised in insect flight.

Following on Dickinson's work on dynamically scaled experiments and Zhang's compliant tramission system, Lynch et al. sought to analyze the effect of elastic element within insect flight kinematic [14]. The physical apparatus build closely resembles that of Dickinson's, but with an addition of an torsional spring serially connected to the flapping wing. Their work establishes a general framework for analyzing forced spring-wing systems that govern oscillatory

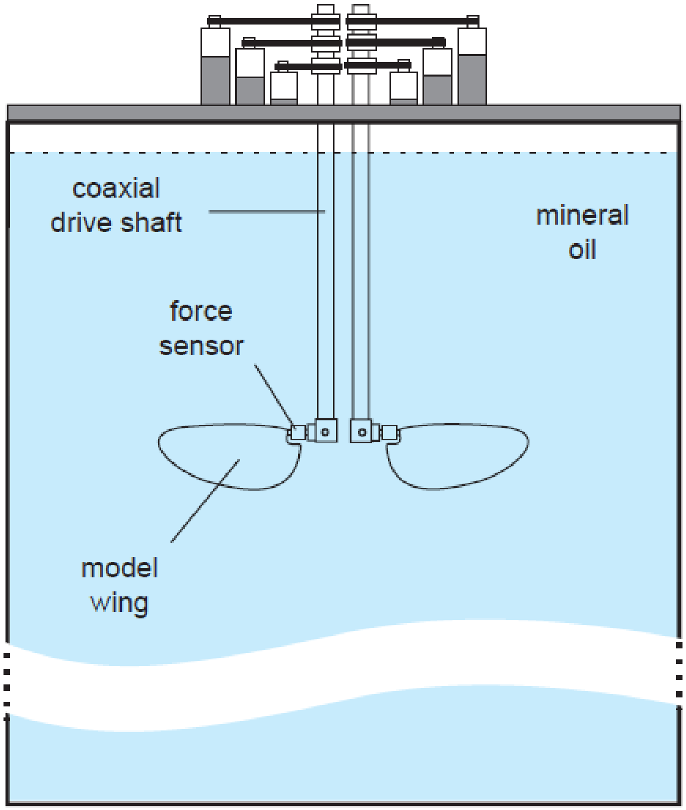

Figure 1.8. The robotic fly apparatus built to investigate the translational and rotational mechanisms that made different insect flight kinematic possible. From [4]

behaviour and dynamic efficiency.

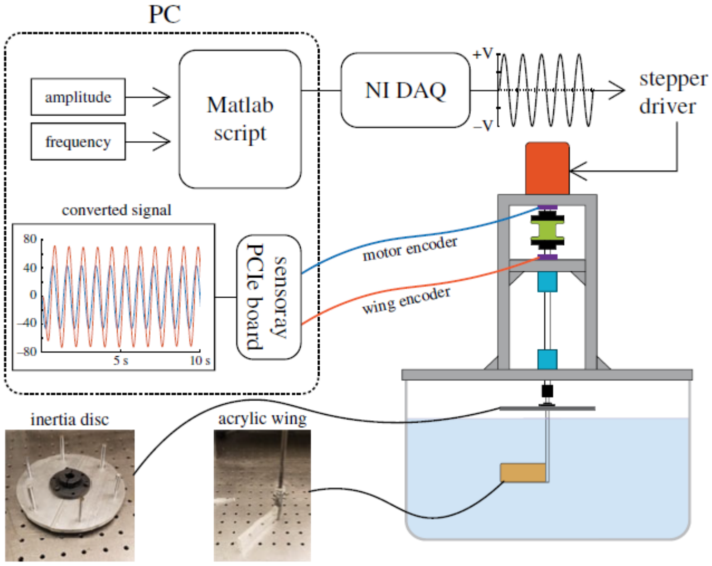

Figure 1.9. A dynamically scaled robophysical flapping model with an elastic element and biologically relevant structural damping. Experiments aimed to elucidate the roles of body mechanics, aerodynamics and actuation in spring-wing energetic. From [14]

Chapter 2

System Overview

To better analysis the effect of wing pitching on flight dynamics, we built a dynamically scaled physical system to mimic the kinematics of insect wing stroke motion. We modified the robophyscical flapping wing system, or RoboFlapper for short, from [[14]] as a foundation of our work. An actuator is integrated into the system for controlling the pitch of the wing. Numerical simulation based on quasi-static modelling was performed to predict and verify the results of our experimentation.

2.1 Robophysical system

As mentioned previously, the basis of the work done for this thesis is based on the RoboFlapper from [14]. The system was originally built to imitate the effect of elastic element within the insect thorax and analyze the benefits of resonance as a kinematic property. In this study, we focus on analyzing the effect of pitch during wing stroke kinematics. As such, a stepper motor is added to the RoboFlapper to achieve active pitching. Figure 2.1 presents the modified system with the two motor design, each corresponding to a degree of freedom. The first is the rotational angle of the whole system, which corresponds to the stroke plane of actual insect flight. In this study it is generally referred to as the flapping angle, and denoted as θ. The second degree of freedom is the pitching angle of the wing, denoted as ϕ. In the actual experiment, the pitching angle is enforced by a stepper motor, which will be discussed in more detail in Chapter 3.

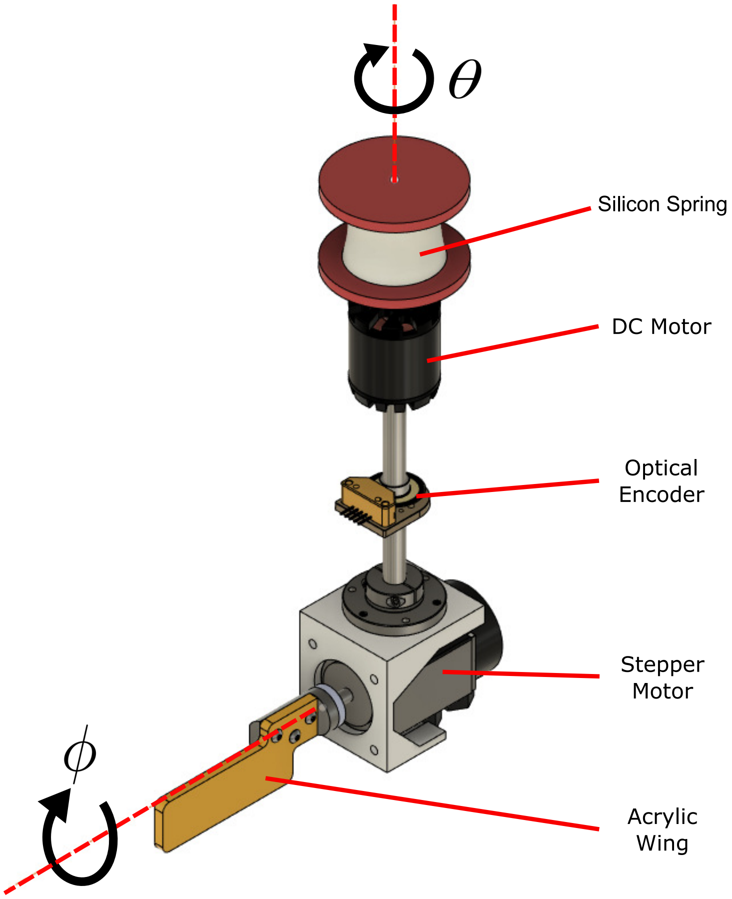

Figure 2.1. The modified RoboFlapper. The system has two degrees of freedom, the flapping angle θ and pitching angle ϕ

The system is characterized as a forced harmonic oscillator consisting of a rotating mass with inertia I and a torsion spring with stiffness K. Its Based on a quasi-static model, the system dynamic is governed by the equation:

$$\ddot{\theta} = \frac{1}{I}(\tau(t) - K\theta - F_D) \tag{2.1}$$

Where $\tau(t)$ is the torque input from the DC motor, $K\theta$ is the elastic spring force, and F_D is the nonlinear fluid drag.

2.2 Input Modulation

From previous studies, we know that wing pitching is a crucial mechanism in flapping wing kinematic in achieving complex locomotion[4]. Within the scope of this thesis, we study the effect wing pitch has on wing stroke amplitude, and estimate from it the effect of drag and production of lift. There are two input signal that we modulate: the output torque from the DC motor, τ, and the commanded position of the pitch angle, ϕ. They are represented in equations form as:

$$\tau(t) = A_\tau \sin \omega t \tag{2.2}$$

$$\phi(t) = A_p \sin(\omega t + \Delta) \tag{2.3}$$

The input signals are chosen to be sinusoidal to mimic the natural movement of insect wings mapped to the stroke plane. The frequency ω of both signal are equal to each other, and are kept constant for each test. The torque magnitude from the DC motor is selected to produce the desired fluid flow condition, detailed in the next section. This is a significant departure from previous work, where the amplitude was enforced. By implementing torque control, we can better analyze the explicit kinematic of wing strokes under the effect of the spring. The amplitude of the pitch signal represent the max wing pitch during a single oscillation cycle of the RoboFlapper. The value is chosen to be mimic the natural behavior of wing pitch motion for insect during hover[18]. Lastly, Δ represent the imposed phase difference between the two input signal. Figure 2.2 illustrate the wing pitch motion mapped to a flat stroke plane of a few key phase differences. As the wing strokes from right to left, the drag profile of the wing changes due to the changing pitch. For example, at $\Delta = \frac{\pi}{2}$ is how wings pitches intuitively, as aerodynamic drag forces pushes the trailing edge opposite the stroke motion. With active pitch control, we can mechanically manifest different kind of pitching scenario and observe the effect it has on wing stroke kinematic.

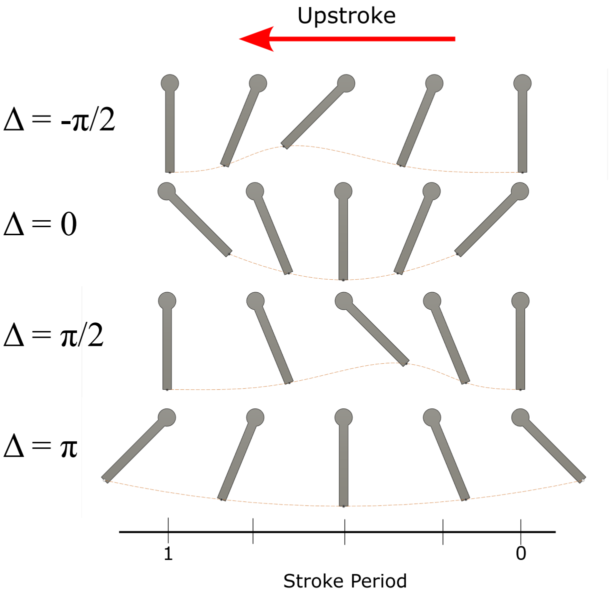

Figure 2.2. Example of wing pitch motion under different phase difference. The leading edge, which is also the rotational axis of the wing, is marked with a circle.

2.3 Dynamic Scaling

To ensure that we match the aerodynamic behaviour of small insect wings, we chose experimental parameters to dynamically scale our system. Consistent with previous dynamically scaled experiments [14], we sought to maintain a Reynolds number in the range of that of small flapping-wing insects, around Re = 100 to 10,000. Reynolds number for a flapping wing is a function of the mean velocity of the wing tip, $\overline{U}$, the mean chord length, c,and the kinematic viscosity of the fluid,ν:

$$Re = \frac{\overline{U}}{c\nu} \tag{2.4}$$

where the mean velocity of the wing tip can be approximated as:

$$\bar{U} = 2LA_w\omega \tag{2.5}$$

where L and A_w is the length and area of the wing respectively, and ω is its angular velocity. We choose water as the working fluid (ρ = 997 kg m^{-3}) and choose wing geometry (rectangular, 10 × 3.3 × 0.63 cm) and a range of actuation parameters (0.5N torque amplitude, 0.2–1.3 Hz frequency) where the resulting wing kinematics is estimated to have Re $= 10^3 - 10^4$. Note that since the wing stroke amplitude is an emergent property of the system due to the series spring configuration, so too is the Reynolds number of an individual test.

Chapter 2, in part, is based on the work from Dimensional analysis of spring-wing systems reveals performance metrics for resonant flapping-wing flight. By Lynch, James and Gau, Jeffrey and Sponberg, Simon and Gravish, Nick. The work of this thesis utilized the apparatus constructed from the aforementioned paper.

Chapter 3

Simulation

Numerical simulation of the quasi-static model based on 2.1 is developed to analyze and predict kinematic behavior of the system. The method used in this paper is based on similar approaches done is [19]. The system dynamic is simulated in MATLAB Simulink based on a spring-mass-damper model.

3.1 Blade Element Method

From 2.1, the only force not explicitly defined is the nonlinear drag force F_D. To approximate the drag force, and similarly the lift produced, we use the blade element method, or BEM, based on works done in [6], [22]. This method allow us to calculate, with sufficient confidence, the nonlinear drag force experienced by the wing. As shown in Figure 3.1, the wing is divided into 30 squares of the same area, The drag force induced, and the lift force that the wing produces, over the squares are then integrated together at every instance of the simulation to better capture the dynamic of the system. Note that, unlike most insects, the wingspan of the RoboFlapper is nearly double its actual wing size. This is because of the dimension limitation of the actuator used to control the pitch. Using this method, we approximate the drag and lift force using standard BEM formula:

$$F_L = \frac{1}{2}\rho_w \hat{A} C_L(\phi)\dot{x}|\dot{x}| \tag{3.1}$$

$$F_D = \frac{1}{2}\rho_w \hat{A} C_D(\phi)\dot{x}|\dot{x}| \tag{3.2}$$

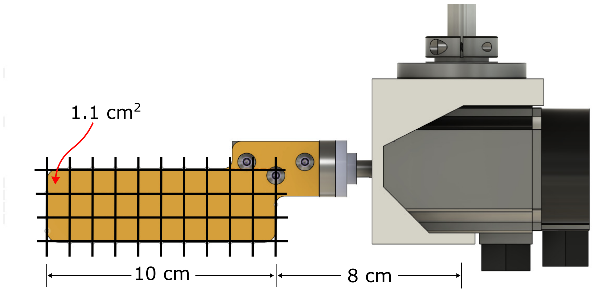

Figure 3.1. Blade Element Method Illustration.

where ρ_w is the density of water, $\hat{A}$ is the area of each square, C_D and C_L are the force coefficients to be discussed in the next section, and $\dot{x}$ is the wing velocity in Cartesian coordinate. Similar to drag force, the wing velocity at each square and are calculated using the equation:

$$\dot{x} = \hat{L}\dot{\theta} + \hat{W}\dot{\phi}cos(\phi) \tag{3.3}$$

where $\hat{L}$ and $\hat{W}$ is the characteristic length and width of the square respectively. Based on the quasi-static model, we only consider the drag force parallel to the stroke plane. As such, the pitching velocity is modified by $cos(\phi)$ to only account for the drag force in that direction. Establishing a geometric relationship between linear velocity and the two radial velocity allow us to better account for trailing edge velocity and its effect on drag.

3.2 Force Coefficient

Equation 3.2 and 3.1 depends on drag and lift coefficient, respectively. The two force coefficients are approximated as function of the pitching angle based on [**?**], shown in figure 3.2. Due to the slight difference in the definition of the coordinate system, the equation for the coefficient are modified accordingly:

$$C_D = 1.9 - 1.5cos(2(\frac{\pi}{2} - \phi)) \tag{3.4}$$

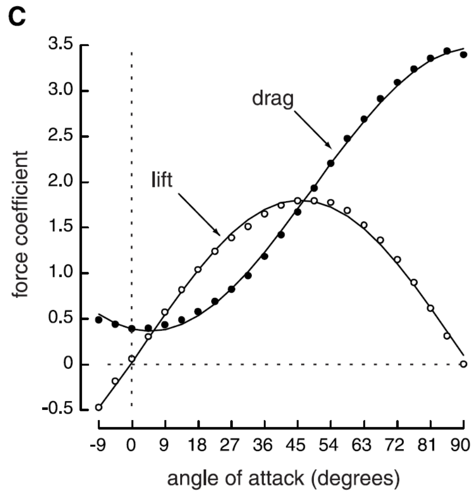

Figure 3.2. Force coefficient estimation from [**?**]. Based on how the coordinate is defined with my system, 45 degree in this figure correspond to 0 degrees in the system.

$$C_L = 1.8sin(2\phi) \tag{3.5}$$

The magnitude of the coefficients based on this approximation matches our intuition. Drag force monotonically increases as the wing pitches closer to the vertical orientation, shown on figure 3.2 as 90 deg. On the other hand, the lift generated maximizes at around 50 degrees. As such, we set the pitch amplitude to be constant at 50 degrees throughout the simulation and subsequent experiments

3.3 Result

Using the model detailed in Ch 2 and approximation in Ch 3, a forced spring-mass-damper system is constructed in Simulink. The parameter used in for the simulation are tabulated in 3.1. The system inertia is experimentally found by performing a frequency sweep of sinusoidal torque inputs on the system using a spring of known stiffness. The frequency at which peak amplitude is achieved is the resonant frequency, which can be used to estimate the system inertia. The stiffness of the spring and wing geometry are selected with experimental consideration, more on that next chapter.

Figure 3.3 present the simulated stroke amplitude result in a color plot. The x axis is the

Table 3.1. A list of system parameter used for this paper

Parameter Name	**Value**	**Unit**
Wingspan length	18	cm
Wing length	10	cm
Mean chord length	3.3	cm
System Inertia	0.013	kg m^2
Spring Stiffness	0.416	Nm/rad
Torque Amplitude	0.5	N
Pitch Amplitude	50	deg
Frequency range	0.2 - 1.3	Hz
Phase difference range	$-\pi$ - π	rad

kinematic phase difference between the flapping and pitching angle, and the y axis is the input signal frequency. From the figure, we can clearly see the effect of system resonance near 0.7Hz. This is less then the expected 0.9Hz natural frequency of the system, due to the effect of drag. Due to non linearity simulation dynamic, the magnitude of the drag force gradually decreases the resonance frequency. In order to better replicate experimental results, the drag force is decreased by one order of magnitude in order for resonance behavior of the system to occur near the natural frequency. This is also the reason that the stroke amplitude are much higher than expected. Still, this amplitude plot reveals a few property of the stroke kinematic that are useful for our analysis. The first the the increasing phase shift of the system as we increase frequency. This is a property of forced harmonic system in general, where increases in input frequency monotonically increase the phasing of the output. The second observation is the repeating pattern of the stroke amplitude every 2π radian phase difference. This is solely a trigonometric relationship, where the signal repeats every 2π.

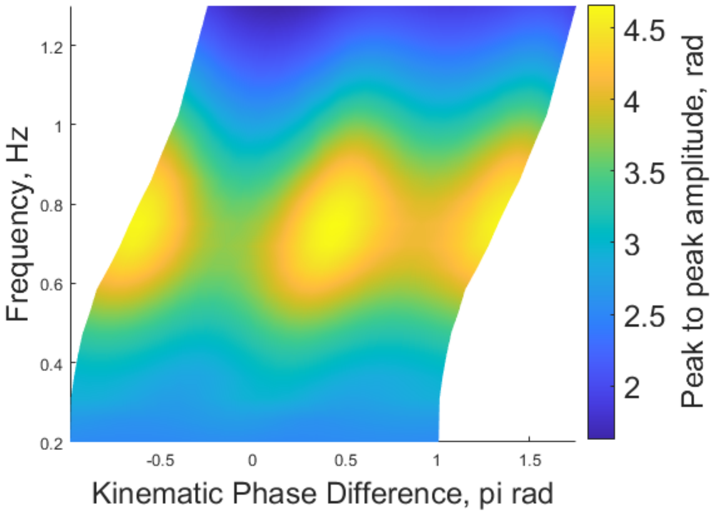

Figure 3.3. Simulated wing stroke amplitude.

More interestingly, however, is why the pattern isn't repeated faster. Figure 2.2 show that the drag profile of the positive and negative phase differences are the same. In other words, the area of the wing perpendicular to the stroke plane at every time instance is the same for kinematic phase difference of $\Delta_k = \frac{\pi}{2}$ and $-\frac{\pi}{2}$. However, we instead see an asymmetry in magnitude in figure 3.3, where the strokes with $\frac{\pi}{2}$ phase difference have a significantly larger amplitude than its counterpart. We hypothesise this phenomenon as a manifestation of the difference in trailing edge velocity. Going back to figure 2.2, we can see that the key difference between the positive and negative phase is in the trailing edge velocity. With a positive phase shift, such as $\Delta_k = \frac{\pi}{2}$, the trailing edge of the wing are behind the leading edge in the direction of the wing stroke.The pitching velocity is acting in the opposite direction of the flapping velocity. The opposite is true with a negative phase shift. For example, with $\Delta_k = -\frac{\pi}{2}$, the two radial velocity compounds together, resulting in the trailing edge behind always ahead of the leading edge. Based on how drag force is calculated using BEM, the higher linear velocity of the negative phase shift parameter will result in a higher drag and thus a lower amplitude.

Base on the simulated dynamic of the system, we calculate the lift generated over one cycle using 3.1. The result is plotted in figure 3.4. We again observe the increasing phase shift and 2π repeating pattern, similar to the amplitude plot. The resonance peaks occur at a higher frequency than that of the natural frequency, which matches results from previous work [9]. There are two prominant ”peaks” to be observed, around $\Delta_k = -\frac{\pi}{2}$ and $\frac{\pi}{2}$. The two extremas are aboust the same in magnitude, but opposite in direction. This is in line with our intuition of how wing works; With a positive phase shift, the trailing edge is behind the leading edge, and the wing pushes the fluid down as it moves across the stroke plane. This creates an upward lift. Vice versa, if the trailing edge is in front, the fluid will be pushed up, inducing a negative lift onto the wing.

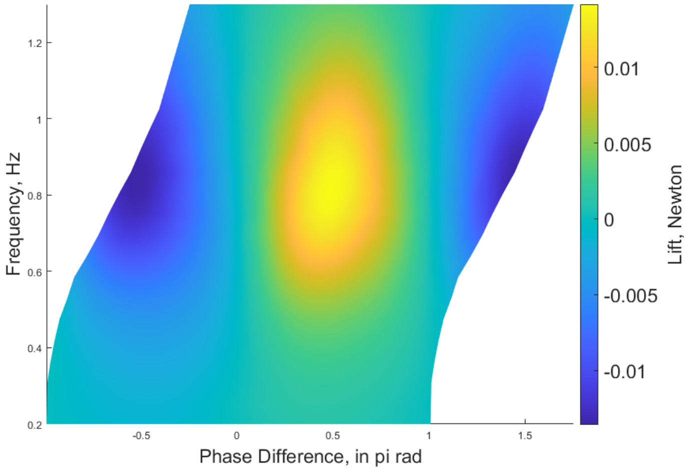

Figure 3.4. Simulated lift generated over one cycle.

Chapter 4

Experiment

With the results of our simulation in mind, we move on to implementing it to the physical RoboFlapper. We will begin by discussing the components of the physical system, leading into how they interface with MATLAB Simulink. The system consists of a DC motor with torque control capability, a moulded silicone torsional spring with linear elasticity and structural damping, an optical encoder for data collection, and a stepper motor with acrylic wing attached for wing pitching. They are attached to a rotary shaft and submerged in a 115-gallon plastic tank filled with water (30” × 30” × 30”, Chem-Tainer). The tank was selected to be large enough to minimize fluid interactions with the side walls, floor and water surface. The wing is situated near the centre of the tank to minimize unwanted dynamic effect. This is consistent with other studies of flapping wings that use water as a working fluid [29–31].

4.1 Equipments

Starting from the top, we have the torsion spring made out of silicone. Silicone was chosen because it can be cast into custom shapes and has a linear elastic response over large strain [33]. The springs were designed with a cylindrical profile with flanges on each end to facilitate coupling to the motor and wing shafts. The stiffness of the spring is around 0.416 Nm rad^{-1}, a value chosen with consideration based on predicted stroke amplitude and torque limit of the DC motor.

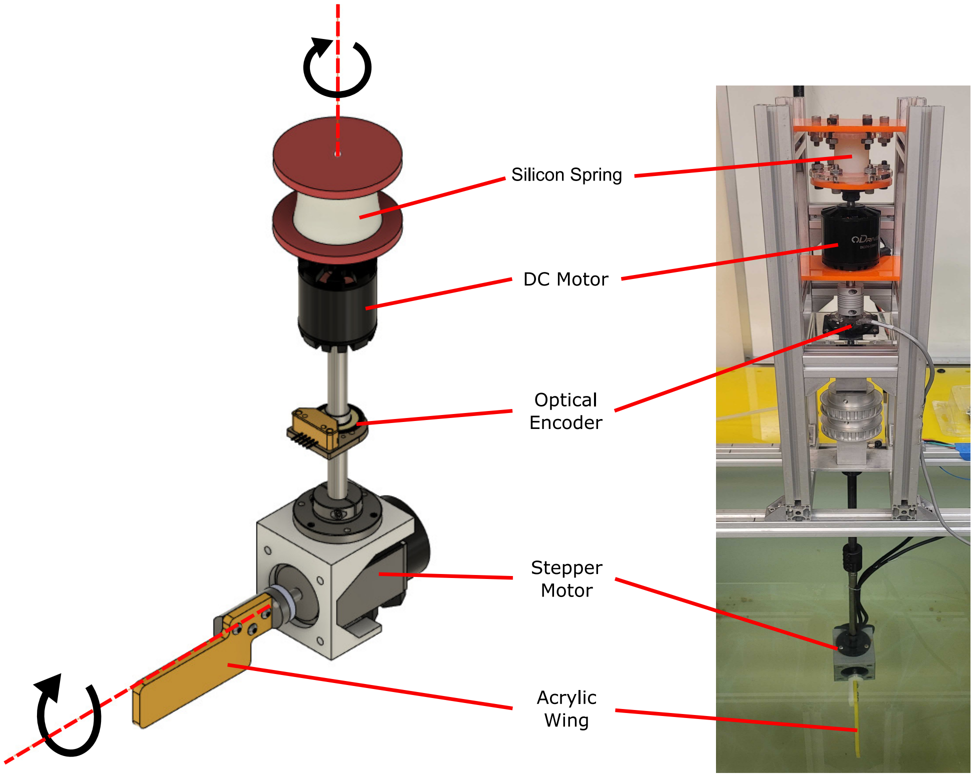

Figure 4.1. Side by side annotation of the RoboFlapper CAD and the real system. Beside the components annotated, the physical system has additional collars and bearings to reduce unaccounted forces.

A DC motor (ODrive Robotics) was chosen to drive the system under closed loop torque control. The motor has a rated torque output of 3.3 Nm, which is significantly more torque than that experienced by the wing when in motion, effectively decoupling the motor and wing dynamics. We monitor the motor angle using an optical encoders (US Digital, 4096 CPR). To reduce the influence of friction on the wing motion, we used two radial air bearings (New Way, S301201)to minimize bearing friction. The shaft is supported vertically by an axial thrust bearing, which contributes some friction. From parametric experimentation, we determine that amount to be significantly small for experimental purposes. [14].

A stepper motor (Stepperonline, P Series Nema 23) is attached to the end of the shaft. It is capable of analog position control with negligible error due to its property. The stepper motor is rated for IP65 waterproof protection. The resolution of the motor is set to be 1600 steps per revolution. The acrylic wing is mounted on to the shaft via a 3D printed mount and a universal motor mount (Pololu, 2693). The wing has an approximate dimension of 10cm by 3.3cm by 0.63cm. It is rectangular with rounded corners to better mimic the assumptions made for BEM.

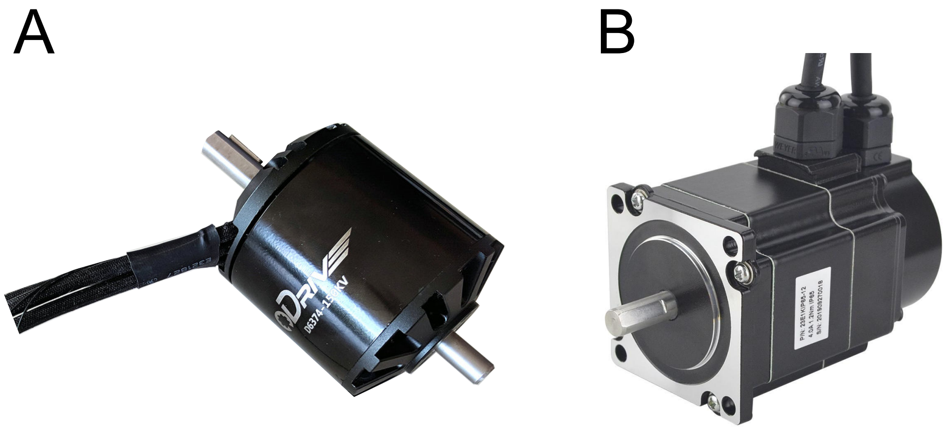

Figure 4.2. Motors used in the physical RoboFlapper. A) is the DC motor that outputs torque that rotationally actuate the system in the θ axis. B) is the stepper motor that control the wing pitch angle, ϕ

To drive the system, voltage is provided to the motors using a 24V power supply, where the power is modulated by their respective drivers. The DC motor driver (ODrive Robotics, v3.6) takes in serial command from the computer and outputs the corresponding voltage to the DC motor for accurate torque control. Similarly, the stepper motor is controlled by the Tic Controller (Pololu, 3140). The PCIe board outputs an analog voltage signal for the controller to perform close loop position control. The conversion between voltage input and position output is calibrated using an external application. Signals from the optical encoder is read by a NI PCIe board (6323 Multifunction IO Device), sampled at 1 kHz. Encoder readings were saved as text files in MATLAB and processed.

4.2 System Parameter

Before beginning the experiment, we have to verify the parameter of the physical system in order to construct a valid model for both simulation and data processing. The first parameter

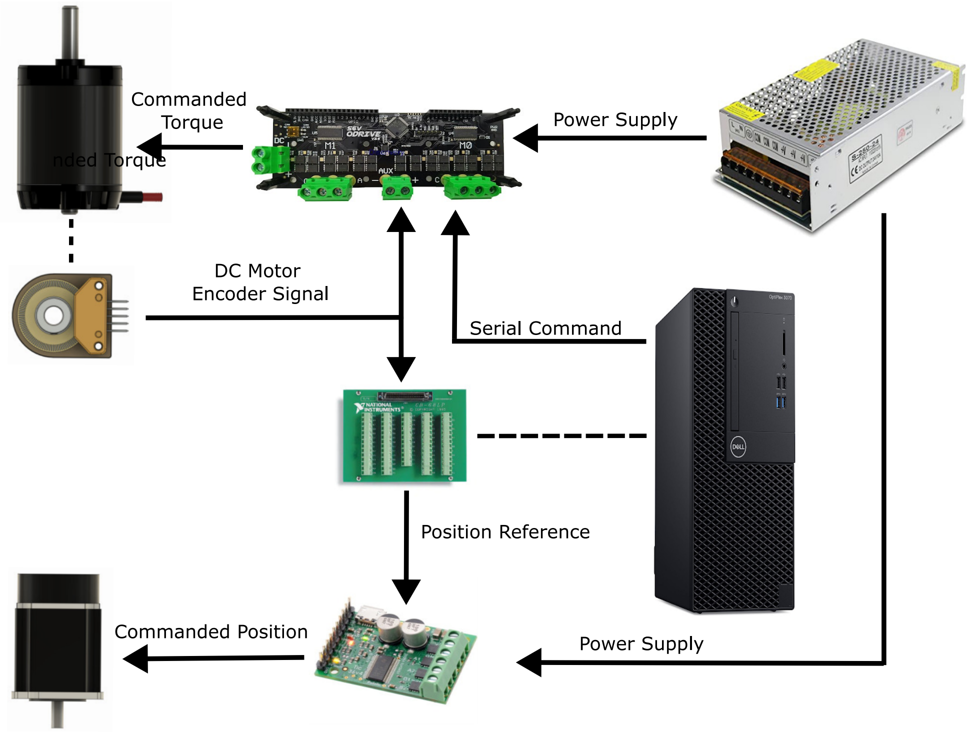

Figure 4.3. Overall circuitry of the system. In essence, the computer commands some user dictates input to the respective drivers for each motor. The data are then collected by the encoder and acquired by the NI DAQ for visualization and logging.

to verify is the rotational stiffness of the silicon spring. In order to estimate the stiffness, we perform a few different set of displacement tests with constant torque input. Assuming the linearity of the silicon spring, the stiffness of the spring is found with:

$$K = \frac{RotationalDisplacement}{InputTorque} \tag{4.1}$$

This experiment is done for a few different springs, of which we chose one with stiffness K=0.416 Nm/rad. Although other springs allow us to operate a wing of larger size at the desired frequency, we are ultimately limited by the small torque output of the DC motor. Our next parameter is the total inertia of the system. Given the elastic nature of our system, we can estimate the system inertia by finding its resonant frequency. By setting the

4.3 Experimental Setup

The experiment begin with the user defining the input signal for the two motors using equations 2.2 and 2.3. Much of the parameter are kept constant through the whole experiment. We only vary the frequency of the signal and the phase shift of $\phi(t)$ to observe the effect of active pitch control on wing stroke kinematic. The equation are then converted into a sinusoidal signal of the within Simulink. We use Simulink Desktop Real-time, or SLDRT, to interface between the software application and the external control boards. SLDRT sent out two commands. The first is a serial command for the ODrive controller telling it the magnitude and direction of torque to output. The second is an analog voltage command to ports on the PCIe board connected to the Tic stepper controller. data read from the PCie board can then be saved and processed on MATLAB, of which the resulting figures below are created. Sufficient time is given between experiments to minimize effects of compound flow. Experimental parameters are chosen at random within pre-determined range to account for system drift. Each experiment is ran for 22 seconds, with a waiting time of about 25 seconds between them.

4.4 Results

The results are based on encoder data read via the PCIe board and processed using MATLAB. Figure 4.5 depicts a sample of the position output from the optical encoder and the stepper motor. Note that the stepper motor signal is the commanded position of the motor shaft, and not its actual position. Although the stepper motor comes with an encoder at the time of purchase, it has since malfunctioned before the final data was collected. Based on previous experience working with this particular motor, we can confidently say that there are negligible difference between the commanded position and the actual position of the motor shaft within the actuation range of this experiment. We sought to repeat the procedures laid out in Ch 3 and observe the effects of active pitch control.

We perform a parameter sweep across the frequency range of (0.2, 1.3) Hz and phase

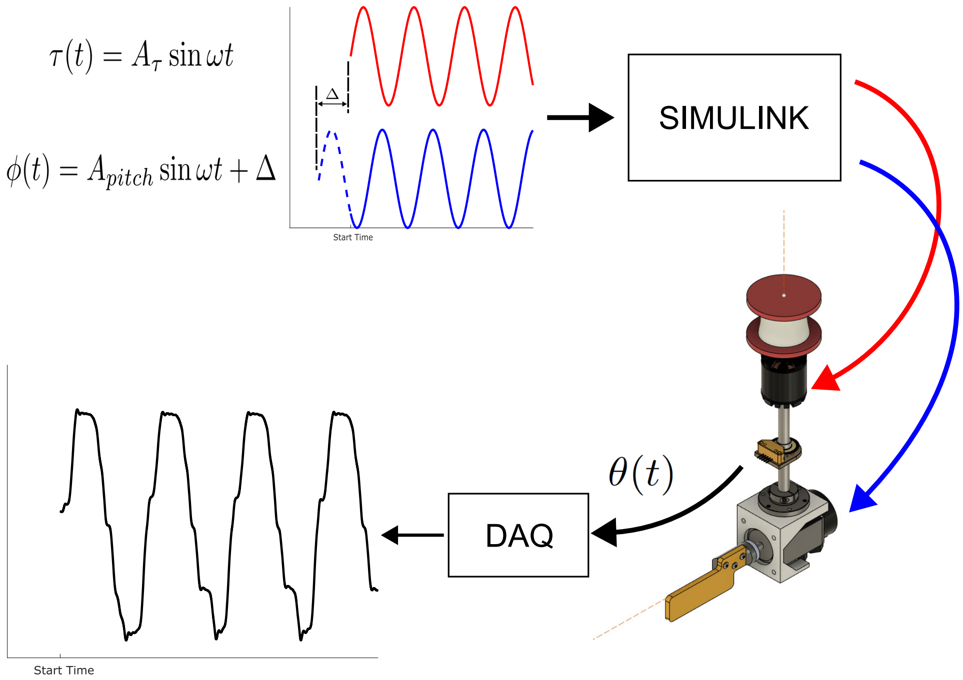

Figure 4.4. The Flow of the experiment The two sinusoidal signals are first processed by MATLAB based on user-defined parameters. It then initialize SIMULINK real time to run on external mode to communicate with the motor drivers. The state of the system are monitored by the encoder, and output signal acquired with the DAQ.

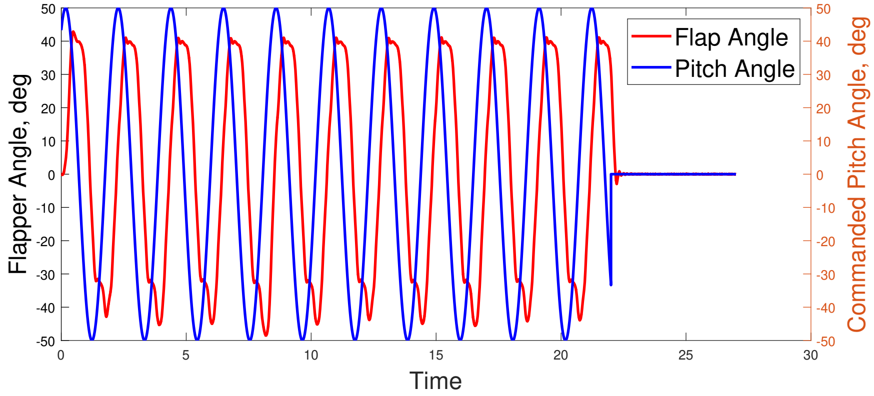

Figure 4.5. Example output reading from the optical encoder, compared with the commanded position of the stepper motor

difference range of (-π, π) rad. The resolution of the parameter sweep is 21 by 25, and takes into consideration the speed and accuracy of the experiment. The wing stroke amplitudes are estimated by measuring the mean difference between maximas and minimas of the flapping angle. We only consider the extremas between 5 and 20 second, a duration that are sufficiently long for the range of frequency used while ensuring a steady state kinematic has been reached. The result of one complete parameter sweep is plotted in 4.6. Each red asterisk on the color plot represent an actual parameter set ran on the RoboFlapper.

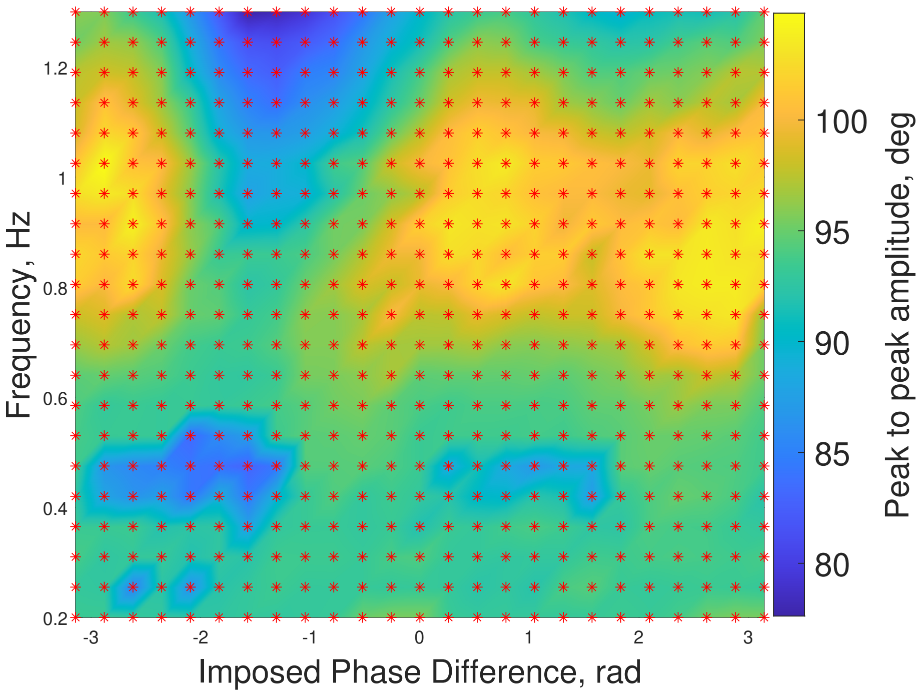

Figure 4.6. Example color plot from a complete parameter sweep

We perform the identical parameter sweep three times total, calculating and producing a plot each similar to 4.6 above. We then take the mean of the three matrices and plot them in 4.7. This gives us an overall smoother result for better analysis. Figure 4.8 plots the standard deviation between the tree parameter sweeps, with the color bar normalized by the amplitude at that point. The STD is below 5 percent of the stroke amplitude around the resonant frequency, proving that the system performance is robust and repeatable.

As mentioned in our modelling, the wing stroke amplitude is an emergent property of the system. We have been plotting the experimental result against the imposed phase difference of Δ that was inputted into the system. However, it was be more revealing to know the actual

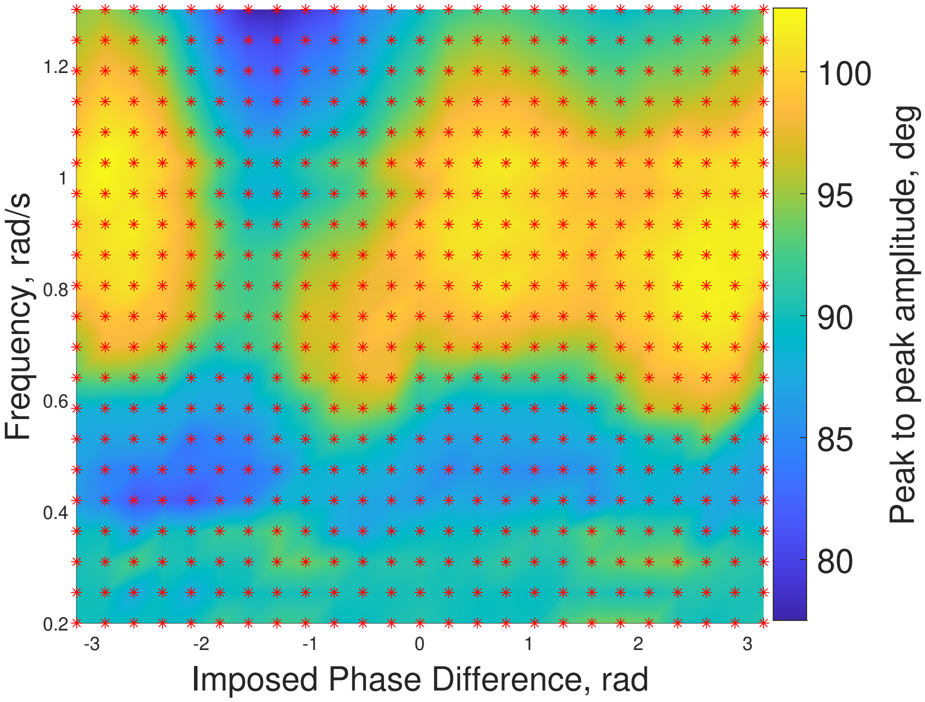

Figure 4.7. Color plot of the mean wing stroke amplitude. The mean is calculated using the estimated stroke amplitude from three separate parameter sweeps. Each red asterisk on the color plot represent a parameter pair.

kinematic phase difference between the flap angle and the pitch angle, Δ_K. We calculate the phase delay between the input torque and the output position for each data point, and add in the additional delay into 4.7. The result is figure 4.9. The x axis is now the estimated kinematic phase difference between θ and ϕ, measured in π radians. The y and z axis is still in the same unit, Hertz and degree respectively. The additional phase delay introduces a gradual shifts in the positive phase direction as frequency increases. This is in line with the properties of elastic systems, where higher frequency generally induces a positive phase shift. On the other hand, effects of the phase difference on additional phase delay is not apparent in our result. Similar to the simulated amplitude plot, there exist a 2π repeating pattern across the phase difference. The asymmetry between positive and negative phase differences can also be found around resonance at $\Delta_K = -0.3$ and 0.7 radian. The resonant peak 0.8-0.9 Hz occurs near the natural frequency of the system. The lift force generated over one cycle is approximated using the same method

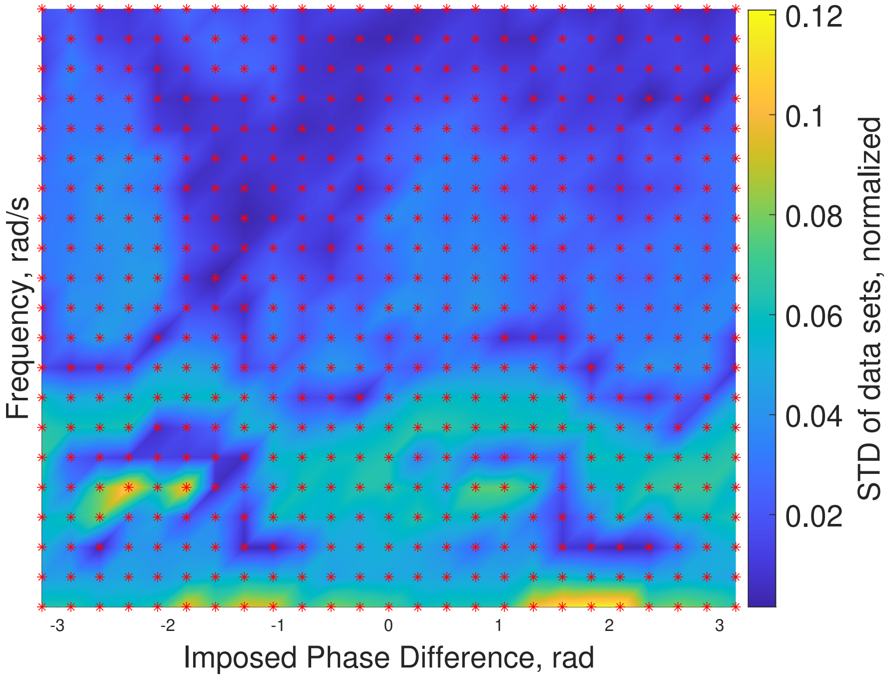

Figure 4.8. Color plot of the standard deviation of wing stroke amplitude between the three parameter sweeps.

detailed in Ch 3, and the result is shown in figure 4.10. We see two peaks of the same magnitude but opposite in direction near the $\Delta_K = -0.5$ and 0.5. This correspond to the first and third row of figure 2.2, where the the positing of the trailing edge relative to the wing dictates the direction of lift generated. The resonant peaks of the lift plot occurs higher than the amplitude resonance, which is also a feature in the simulated results.

4.5 Discussion

From both the simulated and experimental result, we can see that same phenomenon of asymmetrical stroke amplitude between phase differences with the same stroke profile. We hypothesised that this is due to the the effect of trailing edge velocity differing between the two scenarios. To test our hypothesis, we fabricate and mount a new acrylic wing with its rotational axis in the middle of the chord onto the stepper motor. This will make the wing kinematically

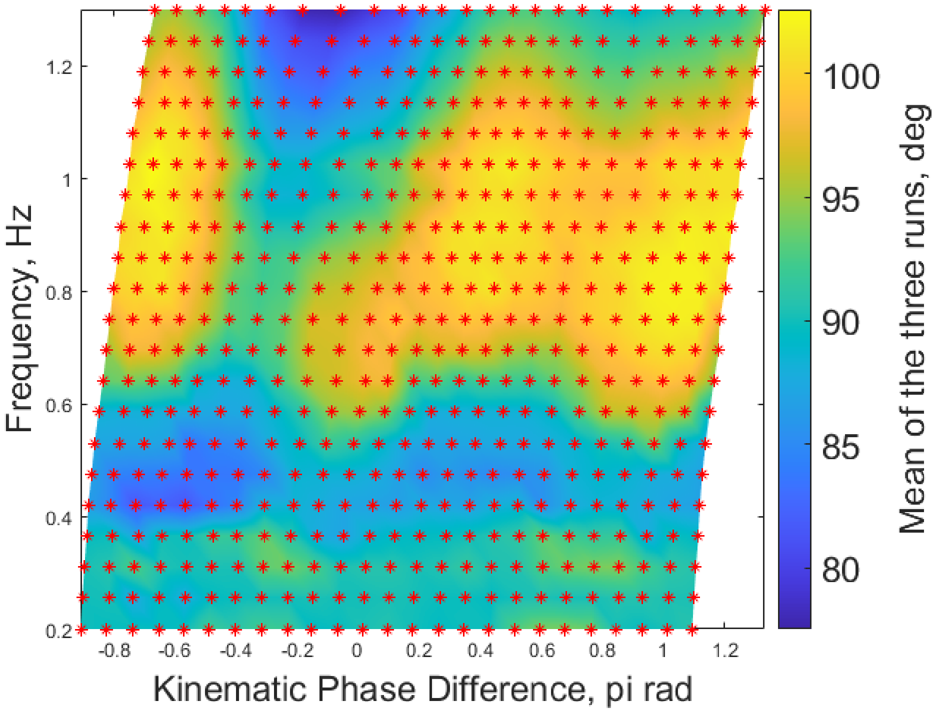

Figure 4.9. Mean stroke amplitude plot, with kinematic phase difference as the x-axis

symmetrical along its length by removing the distinction of leading and trailing edge. The result of a phase sweep across the resonance frequency is shown in figure 4.11. As we predicted, the stroke amplitude curve is approximately symmetric about 0 phase difference. This confirms out hypothesis of the trailing edge effect. There are a few limiting factors of the experiment, of which the biggest issue is with the size and mass of the stepper motor. It was experimentally approximated that the stepper motor contributes to 15 percent of the total system inertia. That in itself is not significant, but we also have to consider the increase in wingspan due to its presence. Under experimental configuration, the wing length it self is only 10 cm, and it is an additional 8cm away from the rotational axis of θ. In order for the dynamic scaling condition to hold, the size of the wing are greatly limited. This is the reason why stroke amplitude varies less then 10 percent across the range of phase difference swept. The effects of active pitch control are greatly diminished due to the relative less variation in drag force.

Furthermore, we neglected to include the additional inertia due to the fluids bounded

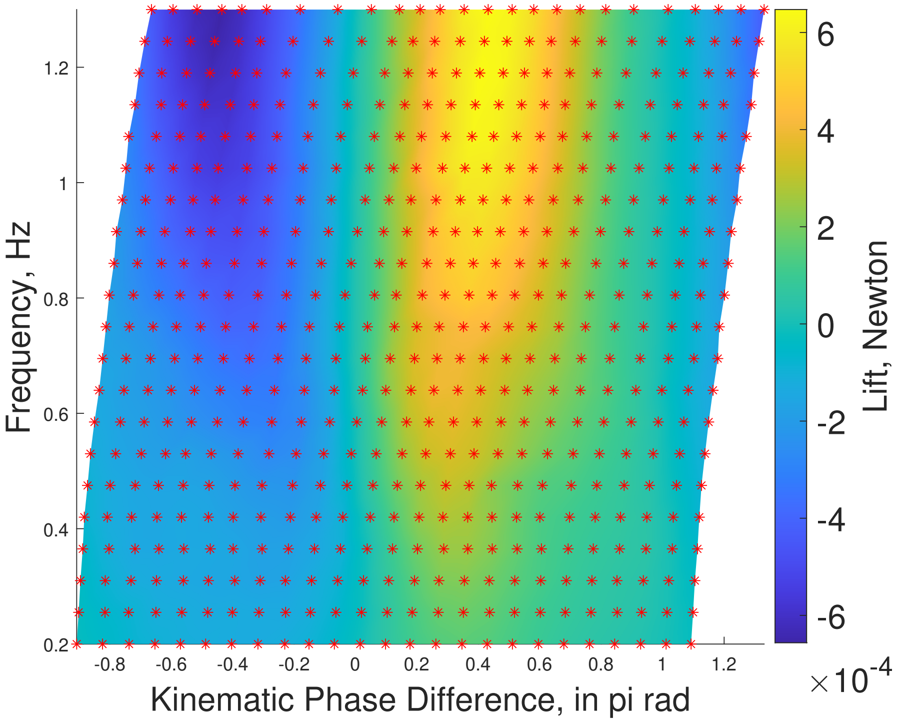

Figure 4.10. Approximated lift generated over one cycle. Values calculated using BEM.

around the wing. This was only discovered after the experiment, when frequency sweep of the system at fixed pitch angle revels a shifting resonance peak. This further amplify the issue of an extended wing by having a significant amount of mass further away from the axis of rotation. We also tried going beyond the Reynolds Number limit for insect flight by using a larger wing. This poses two issues. The first is the dimension of the tank used. In order to assume free stream fluid flow, the wing have to operate at a sufficient distance away from the walls and surface of the tank. This limits the overall dimension of the wing. Additionally, a larger wing area increases the system inertia drastically with the greater fluid mass that bounds to it. In order to operate the DC motor at its rated frequency near the predicted resonance, we have to use a stiffer spring. We soon discover that the DC motor is not capable of outputting a high enough torque if we wish to operate with a resonance frequency of 1 Hz with a larger wing and stiffer spring.

Chapter 4, in part, is based on the work from Dimensional analysis of spring-wing

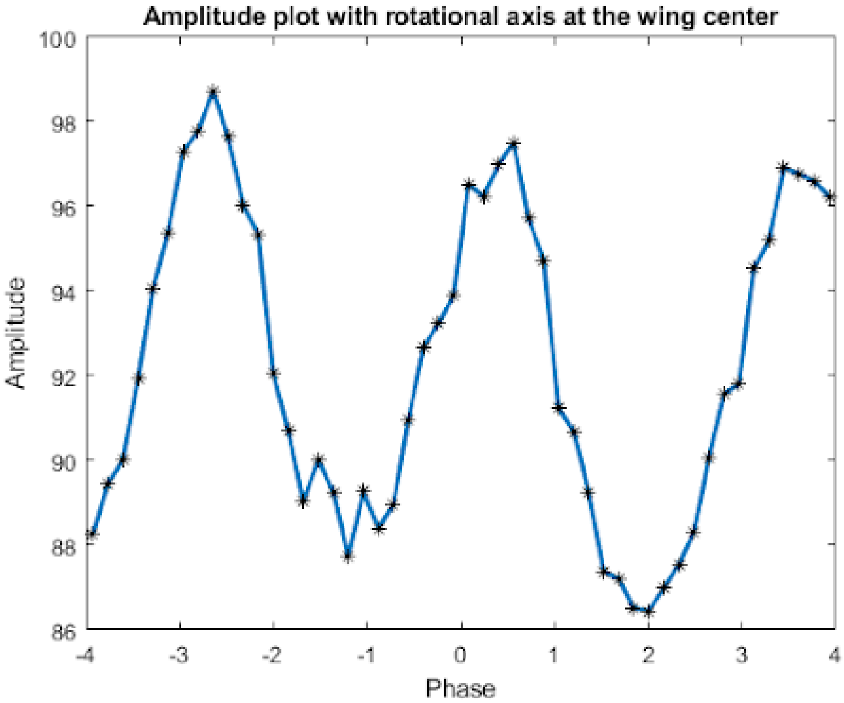

Figure 4.11. Plot depicting the symmetry between positive and negative phase difference when the rotational axis of the wing is at the middle. As we no longer have distinction between the leading and trailing edge, the asymmetry we see in the experimental and simulated result disappears.

systems reveals performance metrics for resonant flapping-wing flight. By Lynch, James and Gau, Jeffrey and Sponberg, Simon and Gravish, Nick. The work of this thesis utilized the apparatus constructed for this paper.

Chapter 5

Conclusion

In this work, we have developed a approximate numerical model for analyzing the effect of actively controlling the pitch during wing-stroke motion. Using conventional estimation for lift and drag, we were able to approximate the stroke kinematics of a dynamically scaled up insect wing. Pitch control capacity is integrated into an existing robotic flapping wing apparatus with a stepper motor. Through open-loop control, we found the variation in effective drag and lift profile when changing the kinematic phase difference between the wing pitch and flapping position. Further work on closed-loop control of the system using phase-modulated oscillators can prove to be invaluable at approximating complex flight locomotion. We hope to apply the knowledge gained using a dynamically scaled up model of a insect wing onto an at-scale FWMAV in the future.

Bibliography

[1] Henry Bennet-Clark. The first description of resilin. *Journal of Experimental Biology*, 210(22):3879–3881, 2007.

[2] Tianxin Cao and J-P Jin. Evolution of flight muscle contractility and energetic efficiency. *Frontiers in Physiology*, 11:1038, 2020.

[3] David Colmenares, Randall Kania, Wang Zhang, and Metin Sitti. Compliant wing design for a flapping wing micro air vehicle. In *2015 IEEE/RSJ international conference on intelligent robots and systems (IROS)*, pages 32–39. IEEE, 2015.

[4] Michael H Dickinson, Fritz-Olaf Lehmann, and Sanjay P Sane. Wing rotation and the aerodynamic basis of insect flight. *Science*, 284(5422):1954–1960, 1999.

[5] Michael H Dickinson and John RB Lighton. Muscle efficiency and elastic storage in the flight motor of drosophila. *Science*, 268(5207):87–90, 1995.

[6] Charles Porter Ellington. The aerodynamics of hovering insect flight. i. the quasi-steady analysis. *Philosophical Transactions of the Royal Society of London. B, Biological Sciences*, 305(1122):1–15, 1984.

[7] Dario Floreano and Robert J Wood. Science, technology and the future of small autonomous drones. *nature*, 521(7553):460–466, 2015.

[8] Jeff Gau, Nick Gravish, and Simon Sponberg. Indirect actuation reduces flight power requirements in manduca sexta via elastic energy exchange. *Journal of the Royal Society Interface*, 16(161):20190543, 2019.

[9] Crawford H Greenewalt. The wings of insects and birds as mechanical oscillators. *Proceedings of the American Philosophical Society*, 104(6):605–611, 1960.

[10] Lindsey Hines, Domenico Campolo, and Metin Sitti. Liftoff of a motor-driven, flapping-wing microaerial vehicle capable of resonance. *IEEE Transactions on Robotics*, 30(1):220–232, 2013.

[11] Noah T Jafferis, E Farrell Helbling, Michael Karpelson, and Robert J Wood. Untethered flight of an insect-sized flapping-wing microscale aerial vehicle. *Nature*, 570(7762):491–495, 2019.

[12] Robert K Josephson, Jean G Malamud, and Darrell R Stokes. Asynchronous muscle: a primer. *Journal of Experimental Biology*, 203(18):2713–2722, 2000.

[13] Matthew Keennon, Karl Klingebiel, and Henry Won. Development of the nano hummingbird: A tailless flapping wing micro air vehicle. In *50th AIAA aerospace sciences meeting including the new horizons forum and aerospace exposition*, page 588, 2012.

[14] James Lynch, Jeff Gau, Simon Sponberg, and Nick Gravish. Dimensional analysis of spring-wing systems reveals performance metrics for resonant flapping-wing flight. *Journal of the Royal Society Interface*, 18(175):20200888, 2021.

[15] James Lynch, Jeff Gau, Simon Sponberg, and Nick Gravish. Autonomous actuation of flapping wing robots inspired by asynchronous insect muscle. In *2022 International Conference on Robotics and Automation (ICRA)*, pages 2076–2083. IEEE, 2022.

[16] Kevin Y Ma, Pakpong Chirarattananon, Sawyer B Fuller, and Robert J Wood. Controlled flight of a biologically inspired, insect-scale robot. *Science*, 340(6132):603–607, 2013.

[17] JE Molloy, V Kyrtatas, JC Sparrow, and DCS White. Kinetics of flight muscles from insects with different wingbeat frequencies. *Nature*, 328(6129):449–451, 1987.

[18] Sanjay P Sane. The aerodynamics of insect flight. *Journal of experimental biology*, 206(23):4191–4208, 2003.

[19] Sanjay P Sane and Michael H Dickinson. The aerodynamic effects of wing rotation and a revised quasi-steady model of flapping flight. *Journal of experimental biology*, 205(8):1087–1096, 2002.

[20] Douglas M Swank. Mechanical analysis of drosophila indirect flight and jump muscles. *Methods*, 56(1):69–77, 2012.

[21] Torkel Weis-Fogh. A rubber-like protein in insect cuticle. *Journal of Experimental Biology*, 37(4):889–907, 1960.

[22] Torkel Weis-Fogh. Energetics of hovering flight in hummingbirds and in drosophila. *Journal of Experimental Biology*, 56(1):79–104, 1972.

[23] Torkel Weis-Fogh. Quick estimates of flight fitness in hovering animals, including novel mechanisms for lift production. *Journal of experimental Biology*, 59(1):169–230, 1973.

[24] Robert J Wood. The first takeoff of a biologically inspired at-scale robotic insect. *IEEE transactions on robotics*, 24(2):341–347, 2008.

[25] Jian Zhang and Xinyan Deng. Resonance principle for the design of flapping wing micro air vehicles. *IEEE transactions on Robotics*, 33(1):183–197, 2017.